Supplementary Materials for

Interglacial instability of North Atlantic Deep Water ventilation

Eirik Vinje Galaasen*, Ulysses S. Ninnemann, Augustin Kessler, Nil Irvalı, Yair Rosenthal, Jerry Tjiputra, Nathaëlle Bouttes, Didier M. Roche, Helga (Kikki) F. Kleiven, David A. Hodell

*Corresponding author. Email: eirik.galaasen@uib.no

Published 27 March 2020, *Science* **367**, 1485 (2020)
DOI: 10.1126/science.aay6381

This PDF file includes:

Other Supplementary Material for this manuscript includes the following:
(available at science.sciencemag.org/content/367/6485/1485/suppl/DC1)

Data S1 (.xlsx)

Materials and Methods

Sample processing and *C. wuellerstorfi* stable isotopes

The International Ocean Drilling Program (IODP) Site U1305 intervals spanning Marine Isotope Stage (MIS) 7e, 9e, and 11c were identified from the stable isotope stratigraphy of Hillaire-Marcel et al. (*39*) and continuously subsampled at 2-cm spacing at the IODP Bremen Core Repository by the curatorial staff. Bulk sediment samples were kept in deionized water on a shaker for 12 hours for disaggregation before being wet sieved using a 63 μm mesh sieve to separate the fine (<63 μm) and coarse fraction material (>63 μm). Following wet sieving, samples were dried at 50°C.

Epibenthic foraminifera *Cibicidoides wuellerstorfi* (*sensu stricto*) shells (Fig. S1) were selectively picked from the >150 μm sediment fraction for stable isotope analyses. The stable isotope analyses were performed at the Facility for advanced isotopic research and monitoring of weather, climate and biogeochemical cycling (FARLAB), Department of Earth Science, University of Bergen, Norway, on a Finnigan MAT 253 mass spectrometer coupled to an automated Kiel IV preparation line kept at constant 70°C. Measurements were performed on one to three individual *C. wuellerstorfi* shells, depending on availability and size, and duplicated per sample when possible (~64% of the samples analyzed). Fig. S2 shows the *C. wuellerstorfi* stable isotope results from Site U1305 including all individual data points. We used Carrera Marble (CM12) as a working standard measured parallel to the foraminifera samples, and all values are reported relative Vienna Pee Dee Belemnite (VPDB) calibrated using National Bureau of Standards (NBS) standard NBS 19 and NBS 18. The long-term reproducibility (1σ) of in-house standards over the analysis period was ≤0.08‰ and ≤0.04‰ for $\delta^{18}O$ and $\delta^{13}C$, respectively. The standard cleaning step for foraminiferal stable isotope analyses, involving methanol and ultrasonication, was avoided to retain mass and increase the number of measurements possible, as *C. wuellerstorfi* shells were generally few and small in size, often providing a total weight at the lower limit possible for analysis (~10-15 μg). Instead of performing the standard cleaning step, *C. wuellerstorfi* tests were visually cleaned using a brush and deionized water ('brush-cleaned') to remove any foreign material on or within them prior to stable isotope analyses. To test the impact of omitting the standard cleaning step, we measured surplus shells from samples (n=22) containing sufficient mass that were cleaned following standard protocols ('standard-cleaned') for removing fine-grained material: adding methanol to reaction vials containing the shells and keeping them in an ultrasonic bath for 10 seconds before extracting the methanol. The $\delta^{18}O$ and $\delta^{13}C$ values of the 'standard-cleaned' *C. wuellerstorfi* tests are very similar to the sample average of the 'brush-cleaned' tests (Fig. S1). Further, the intra-sample reproducibility of the 'brush-cleaned' Site U1305 *C. wuellerstorfi* $\delta^{18}O$ and $\delta^{13}C$ data is similar to a large data set of exclusively 'standard-cleaned' *C. wuellerstorfi* shells from the same region (the MIS 5e section of MD03-2664; location shown in Fig. 1) (Fig. S1). This indicates that the visual 'brush-cleaning' and 'standard-cleaning' steps performed similarly well with no discernible difference in the stable isotope values or in the intra-sample variability. Nonetheless, performing the standard cleaning step for foraminiferal stable isotope analyses is highly recommended when possible. Indeed, in certain regions and time intervals, a cleaning procedure more stringent than the standard one is likely required to accurately determine foraminiferal stable isotope values (*40*).

C. wuellerstorfi B/Ca

We measured B/Ca ratios in *C. wuellerstorfi* tests from intervals in MD03-2664 (MIS 5e) and Site U1305 (MIS 7e, 9e, and 11c). To obtain sufficient mass for B/Ca analyses (~250-300 μg), and due to scarcity of *C. wuellerstorfi* tests in these sediments, it was often necessary to combine tests from up to a maximum of six adjacent samples (or 12 cm of core) that we restricted according to consistent *C. wuellerstorfi* $\delta^{13}C$ values. Following the selective picking, the *C. wuellerstorfi* tests were opened using clean glass slides and transferred into acid-leached vials. The *C. wuellerstorfi* tests were subsequently cleaned for contaminating phases, including clay removal, reductive and oxidative steps, a weak acid leach, and dissolution in dilute HNO_3. The B/Ca analyses were performed using the method outlined in Rosenthal et al. (*41*) on a Finnigan MAT Element XR Sector Field Inductively Coupled Plasma Mass Spectrometer (ICP-MS) at the ICP-MS laboratory at the Institute of Marine and Coastal Sciences, Rutgers, The State University of New Jersey, USA.

Site U1305 *N. pachyderma* (s) $\delta^{13}C$ records

N. pachyderma (s) tests were selectively picked from the 150-212 μm sediment fraction at continuous 4-cm spacing across MIS 7e, 9e, and 11c (with notable gaps only in MIS 9e due to scarcity of *N. pachyderma* (s) tests). Prior to the stable isotope analyses, the tests were cleaned by adding methanol to the sample kept in reaction vials and ultrasonicating them for ten seconds before removing the supernatant. The stable isotope analyses were performed at FARLAB, University of Bergen, Norway, as outlined for benthic foraminifera *C. wuellerstorfi* above, and with identical standard reproducibility. Measurements on *N. pachyderma* (s) were replicated whenever possible (~92% of the samples), and each individual measurement was performed on 6-10 individual *N. pachyderma* (s) tests.

Ice-rafted debris

The ice-rafted debris (IRD) counts were performed on the same Site U1305 samples as the benthic foraminiferal stable isotope measurements, but at lower sampling density. IRD counts were performed at 32-cm spacing for MIS 7e and 11c, and 16-cm spacing for MIS 9e (*42*). Following the sample processing steps outlined above, material in the >150 μm fraction were split, IRD grains visually identified, and IRD calculated as the percent of ≥300 counted entities.

Hole U1305C MIS 11c mcd fine-tuning

Sediment physical properties (e.g., magnetic susceptibility) indicated cm-scale offsets between Hole U1305C and the original (Hole A & B) splice over ~74.5-78.5 mcd (Fig. S3A), corresponding to most of MIS 11c. We fine-tuned the mcd scale for the Hole U1305C MIS 11c interval using magnetic susceptibility, shifting it between -3 cm and -19 cm to align the physical property records (Fig. S3B), and include both the original and corrected core depth scales in the MIS 11c data table.

iLOVECLIM model simulation

We used the iLOVECLIM Earth system model of intermediate complexity to simulate and assess potential relationships between NADW distribution, northwest Atlantic bottom water $\delta^{13}C$, and AMOC. The iLOVECLIM model is an isotope-enabled development branch of LOVECLIM version 1.2 (*43*) and includes an ocean component (CLIO) with 20 vertical layers

and 3° by 3° horizontal resolution as well as land and ocean carbon cycle modules (*25*). We performed a transient simulation for 125-115 ky (corresponding to MIS 5e) using annually interpolated greenhouse gas and orbital forcings following the third phase of the Paleoclimate Modelling Intercomparison Project (PMIP; https://pmip3.lsce.ipsl.fr/), initialized from a quasi-equilibrium spin up of 5000 years forced with constant 125 ky boundary conditions. We performed two quasi-equilibrium spin-ups prior to the 125-115 ky simulation, each integrated for 5000 years. The first is based on preindustrial conditions and the second on 125 ky boundary conditions. The preindustrial simulation was used to validate and confirm that iLOVECLIM reproduces the spatial distribution of preindustrial ocean $\delta^{13}C$ (*22*), and the 125 ky spin-up to initialize the 125-115 transient simulation. To test the sensitivity of the simulated deep Atlantic $\delta^{13}C$ variability to changes in surface biological processes and preformed $\delta^{13}C$ values, we ran to additional 125-115 ky transient simulations using similar initial conditions as above but starting at 125 ky with either: 1) atmospheric $\delta^{13}C$ fixed at value decreased by ~0.6‰ (at -7.1‰); or 2) with 50% decreased primary productivity in the modeled convection regions off southern Greenland and in the Nordic Seas. We expand on the model results in the discussion section of the supplement below.

The modeled inorganic carbon cycle is represented by dissolved inorganic carbon (DIC) and alkalinity (ALK), while the organic carbon cycle includes phytoplankton, zooplankton, dissolved organic carbon (DOC), slow dissolved organic carbon (DOCs), particulate organic carbon (POC), and $CaCO_3$. The phytoplankton is partially remineralized as it sinks through the water column, while all the POC and $CaCO_3$ is remineralized at depth. The remineralization profile follows an exponential law, adjusted to have less remineralization in the upper layers and more at depth. Carbon fractionation during photosynthesis fixes ^{12}C in the organic matter, which is added back by the remineralization process at depth. At the air-sea interface, the carbon flux is computed from the CO_2 partial pressure difference between the atmosphere and ocean at a constant gas exchange coefficient of 0.06 mol m^{-2} yr^{-1}, where sea surface pCO_2 is a function of temperature, salinity, DIC, and ALK following Millero (*44*). The modeled $\delta^{13}C$ distribution is thus affected by air-sea gas exchange and organic matter production/remineralization, and transported by the advection-diffusion scheme of the model. Unlike ^{12}C, the atmospheric ^{13}C is prognostically simulated in response to land and ocean processes.

Supplementary Text

Site U1305 age model

The age models for the MIS 7e, 9e, and 11c intervals of Site U1305 were constructed by correlating our benthic $\delta^{18}O$ record to and adopting the age model constructed for ODP Site 983 (*33, 45*) (Fig. 2, Fig. S4). Using Site 983 benthic $\delta^{18}O$ as a tuning target has advantages over other reference records. First, Site U1305 shares well-defined structures in benthic $\delta^{18}O$ with Site 983 (Fig. 2; Fig. S4) allowing relatively robust correlation. Further, high-resolution IRD records are available from both sites and allow us to validate the benthic $\delta^{18}O$-correlation near deglacial intervals where Site U1305 benthic $\delta^{18}O$ data were often lacking due to *C. wuellerstorfi* absence (Fig. 2). Tie points were defined based on major benthic $\delta^{18}O$ transitions and linearly interpolated between to obtain ages for all core depths (Fig. S4). The Site U1305 and MD03-2664 IRD records were also used to guide the determination of tie points at the start of the interglacial $\delta^{18}O$ plateaus, as deglacial IRD increases are observed to coincide with transient decreases in benthic $\delta^{18}O$ values before MIS 5e (*10*) and MIS 7e, 9e, and 11c in this region (Fig.

2; Fig. S4). Given their transient nature and co-occurrence with deglacial IRD, these deglacial benthic $\delta^{18}O$ reductions may reflect contamination from low-$\delta^{18}O$ detrital carbonate commonly deposited during Heinrich-events (*40*). Consequently, deglacial samples with low *C. wuellerstorfi* $\delta^{18}O$ and high IRD were disregarded when we constructed our age model and we defined the first interglacial benthic $\delta^{18}O$ value, and start of the interglacial plateaus, as the first continuously low $\delta^{18}O$ value occurring after large deglacial IRD increases. Corroborating this approach, the Site U1305/MD03-2664 and Site 983 deglacial IRD peaks align using this additional constraint for the benthic $\delta^{18}O$ tuning (Fig. S4) but would otherwise be offset by a few thousand years.

Age uncertainties involved with benthic $\delta^{18}O$-based age models can be considerable. For example, age differences between major $\delta^{18}O$ transitions can reach up to a few thousand years between different ocean basins (*46*). The absolute age uncertainty provided by the Site U1305-Site 983 correlation is likely less than millennial, given i) the relative proximity of these core sites, ii) the similarity of the benthic $\delta^{18}O$ records—indicating a shared $\delta^{18}O$ evolution, and iii) the alignment of deglacial IRD peaks (Fig. 2; Fig. S4). Despite a relatively robust correlation, the original age model still carries considerable uncertainty in absolute ages. For example, adopting a different age model constructed for Site 983 by Barker et al. (*45*) (e.g., EDC3 and AICC2012), would shift absolute ages up to a few thousand years.

In addition to absolute age uncertainties, relative (sample-to-sample) age uncertainties likely also exist for the Eirik Drift (Site U1305 and MD03-2664) records. Correlation of benthic $\delta^{18}O$ records is achieved using a limited number of tie points. This is especially true for interglacial $\delta^{18}O$ plateaus, here defined by two (MIS 5e, 7e, and 9e) or three (MIS 11c) tie points (Fig. 2, Fig. S4). These tie points were linearly interpolated between, assuming constant sedimentation rates. However, interglacial sedimentation rates can vary on a range of timescales in this area (*39, 47-49*). For example, radiocarbon-dated sections indicate that sedimentation rates were higher in the early compared to the late phase of the current interglacial at multiple Eirik Drift locations (e.g., *12, 48*). If this temporal sedimentation pattern persisted in the older interglacial periods, our age models based on the conservative approach of linear interpolation may over- and underestimate the durations of early and late interglacial intervals, respectively.

Site U1304, MD03-2664, MD03-2665, and MD99-2227 age models

To place all proxy records on a common age scale, we revised the age models for all core intervals containing data we compare to the IODP Site U1305 records. We tuned the MIS 5e interval of MD03-2664 and the MIS 5e, 7e, 9e, and 11c intervals of IODP Site U1304 to the same ODP Site 983 reference record (Fig. S4), applying identical tie points and linearly interpolating between as outlined above. The MIS 1 and last deglacial intervals of Site U1304 and MD03-2665 were left on their original age models as presented in Xuan et al. (*38*) and Kleiven et al. (*12*), respectively.

To compare our records to the MD99-2227 southern Greenland sediment discharge reconstructions (*18, 32, 36*), we transferred our benthic $\delta^{18}O$-based age models for MIS 5e (MD03-2664), 7e, 9e, and 11c (Site U1305) to MD99-2227 by correlating magnetic susceptibility between this core and MD03-2664 (MIS 5e) and Site U1305 (MIS 7e, 9e, and 11c) (Fig. S5). The strong similarity of the magnetic susceptibility records indicate that these core sites shared sedimentation histories, providing robust relative age control to comparisons of the Site U1305/MD03-2664 and MD99-2227 records. The alignment of glacial and interglacials values in epibenthic foraminifera *C. wuellerstorfi* $\delta^{18}O$ from MD03-2664/Site U1305 and

planktic foraminifera *N. pachyderma* (s) $\delta^{18}O$ from MD99-2227 on the obtained age models supports the magnetic susceptibility correlation (Fig. S5). Carlson et al.'s (*50*) age model was used for the MIS 1 and last deglacial intervals of MD99-2227.

C. wuellerstorfi B/Ca and *N. pachyderma* (s) $\delta^{13}C$

To test the fidelity of Eirik Drift *C. wuellerstorfi* $\delta^{13}C$ as recorder of bottom water carbon chemistry and water mass tracer, we use epibenthic foraminifera *C. wuellerstorfi* B/Ca, a proxy for bottom water carbonate ion saturation ($\Delta[CO_3^{2-}]$) and independent metric of the influence of high-$[CO_3^{2-}]$ NADW versus low-$[CO_3^{2-}]$ SSW (e.g., *51, 52*). The Eirik Drift *C. wuellerstorfi* B/Ca data span a range of 185-215 µmol/mol with distinct changes within each of MIS 5e, 7e, 9e, and 11c (Fig. S6). Using Yu & Elderfield's (*51*) B/Ca to $\Delta[CO_3^{2-}]$ relationship for *C. wuellerstorfi*, the B/Ca data indicates intra-interglacial changes in bottom water $[CO_3^{2-}]$ by 25-30 µmol/kg, similar to that expected from shifting between NADW and SSW influence (e.g., *52*). The concurrent and coupled changes in *C. wuellerstorfi* $\delta^{13}C$ by up to ~0.8‰ within the same sample pool (Fig. S6) is similarly consistent with shifts between NADW and SSW influence. Indeed, the paired change in Eirik Drift *C. wuellerstorfi* B/Ca and $\delta^{13}C$ we observe is similar to that recorded in the last glacial to Holocene sections of two North Atlantic cores from similar water depths (Fig. S6) that was previously interpreted to reflect the well-established deglacial shift from SSW to NADW influence in the deep North Atlantic (*52*). We suggest that the Eirik Drift *C. wuellerstorfi* B/Ca record supports the interpretation of the *C. wuellerstorfi* $\delta^{13}C$ variability as reflecting changes in NADW versus SSW influence.

An alternative explanation for co-variability in trace element ratios and $\delta^{13}C$ is contamination by secondary $CaCO_3$ precipitation and presence of authigenic overgrowths. However, several lines of evidence argue against a role for contamination by secondary $CaCO_3$ precipitation. The *C. wuellerstorfi* $\delta^{13}C$ record suggest no discernible influence by its own merit, showing for example i) absolute values within the range of values observed in the modern ocean or relevant reconstructions (e.g., *22, 23; Fig. 3*) and ii) a consistency in the signal and a lack of extremely large fluctuations that would require the mass and isotope value of any contamination to have adjusted itself to balance changes in the mass and isotope value of the foraminifera tests. Further, secondary $CaCO_3$ precipitation should, if present, influence all foraminifera tests in a given core depth to some degree similarly. That is, if secondary $CaCO_3$ precipitation drove relatively large changes in *C. wuellerstorfi* $\delta^{13}C$ and B/Ca, planktic foraminifera $\delta^{13}C$ should also show low $\delta^{13}C$ values in addition to some degree of co-variability. The Eirik Drift *N. pachyderma* (s) $\delta^{13}C$ records from MIS 5e, 7e, 9e, and 11c do not show values as low as the *C. wuellerstorfi* $\delta^{13}C$ records and there is no significant relationship between *N. pachyderma* (s) and *C. wuellerstorfi* $\delta^{13}C$ (Fig. S6). In sum, we suggest secondary $CaCO_3$ precipitation is either unimportant or entirely absent and consider it as an unlikely explanation for the co-variability in *C. wuellerstorfi* B/Ca and $\delta^{13}C$. Changes in the influence of NADW versus SSW could conversely explain these observations.

iLOVECLIM model simulation results

We identified persistent centennial-scale variability in $\delta^{13}C$ and the distribution of NADW in our 125-115 ky transient simulation occurring over a ~6 ky long interval in-between intervals of relative stability during the initial 2-3 and final 1-2 ky. A subsequent study will outline and discuss the results of the model simulation in detail (Kessler et al., in prep.). Here, we use the simulation to help the interpretation of the reconstructed bottom water $\delta^{13}C$ variability by

assessing how centennial-scale changes in NADW distribution can impact deep Atlantic $\delta^{13}C$. We focus on the simulated episodes of NADW shoaling and recovery to assess the possible rate, duration, and magnitude of water mass distribution and associated bottom water $\delta^{13}C$ changes and compare these to the reconstructed $\delta^{13}C$ variability. In the simulation, episodes of NADW shoaling were abruptly initiated, lasted some centuries, and were associated with decreases in AMOC strength and North Atlantic bottom water $\delta^{13}C$ (Fig. 4).

The simulated episodes of NADW shoaling/deepening produced distinct North Atlantic bottom water $\delta^{13}C$ variability as (low-$\delta^{13}C$) Southern source water (SSW) expanded/contracted in concert with (high-$\delta^{13}C$) NADW contracting/expanding (Fig. 4). In the northwest Atlantic region corresponding to the location of Eirik Drift core sites U1305, MD03-2664, and MD03-2665, shoaling of NADW and incursions of SSW manifested as ~0.4‰ decreases in bottom water $\delta^{13}C$ achieved over a few decades, events that ended equally abrupt as NADW deepened some centuries (~100-500 years) later (Fig. 4). To illustrate these NADW and $\delta^{13}C$ distribution changes, Fig. 4A and Fig. 4B displays the North Atlantic mean $\delta^{13}C$ distribution below 500 m water depth for all simulated years with anomalously strong AMOC (>2σ; n=460 model years; mean AMOC strength: 16.75±0.70 Sv) and anomalously weak AMOC (<2σ; n=63 model years; mean AMOC strength: 8.00±0.42 Sv), respectively. We further selected two simulated intervals of NADW shoaling and recovering to compare to the reconstructed bottom water $\delta^{13}C$ variability (Fig. 4B), differing from other simulated shoaling episodes only in duration. The magnitude of any bottom water $\delta^{13}C$ variability driven by such changes in the relative influence of northern versus southern source water could depend strongly on the preformed $\delta^{13}C$ of, and the gradient between, competing water masses. While iLOVECLIM captures the preindustrial preformed $\delta^{13}C$ of northern and southern source waters relatively well (e.g., compare Fig. 1 to Fig. 4A), proxy records suggest considerable changes in preformed water mass $\delta^{13}C$ occurred between and even within past interglacial periods. For example, the preformed $\delta^{13}C$ of northern source water may have been higher in the Holocene than the late Pleistocene interglacials (see data composites, purple lines, in Fig. 3), while it likely increased across MIS 5e (Fig. 3) consistent with planktic and epibenthic foraminifera $\delta^{13}C$ records from the Nordic Seas (e.g., *53*). This model-data difference should be noted when comparing and contrasting the simulated and reconstructed time series. For the proxy reconstructions, we took this into account by averaging multiple events in order to illustrate common features independent of specific interglacials and preformed $\delta^{13}C$ values (Fig. 4). Still, the similarity of the modeled and reconstructed bottom water $\delta^{13}C$ changes could result from the simulation having a specific set of preformed $\delta^{13}C$ values in NADW and SSW. To assess how different background states and preformed $\delta^{13}C$ in NADW and SSW could impact the magnitude and character of the simulated bottom water $\delta^{13}C$ variability, we reran the simulation twice with 1) atmospheric $\delta^{13}C$ lowered by ~0.6‰ and 2) 50% decreased primary productivity in the simulated deep water formation regions off southern Greenland and in the Nordic Seas. Both experiments shift the absolute values of the simulated Eirik Drift bottom water $\delta^{13}C$ time series but in both cases the relative magnitudes and character of the variability is only negligibly impacted (Fig. S7). The simulation with perturbed primary productivity, resulting in limited change in deep Atlantic $\delta^{13}C$, supports previous studies suggesting that organic carbon fluxes have little influence on the $\delta^{13}C$ of *C. wuellerstorfi* (e.g., *21*). Thus, the character of the Eirik Drift bottom water $\delta^{13}C$ variability driven by shifts in the distribution of water masses appears to be relatively stable in face of different preformed $\delta^{13}C$ values and background biological processes in the model, indicating that the similarity between the simulated and reconstructed variability is not strongly dependent on the specific model

configuration. That this character is similar to the reconstructed Eirik Drift bottom water $\delta^{13}C$ reductions, including in the magnitude, rate, and duration of events (Fig. 4; Fig. S7), supports the inference that characteristic deep Atlantic $\delta^{13}C$ changes can be explained with changes in the distribution and influence of NADW and SSW.

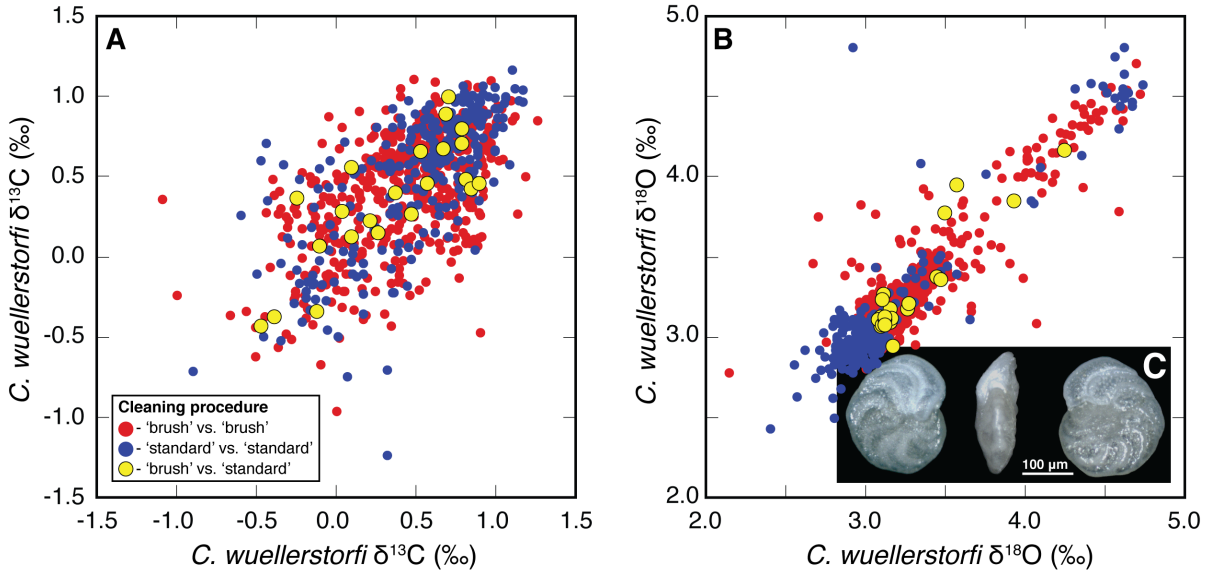

Fig. S1. Eirik Drift *C. wuellerstorfi* (*sensu stricto*) replicate stable isotope values for different cleaning procedures. Cross-plots comparing sample replicate measurements where sufficient *C. wuellerstorfi* tests were present to allow it (n=493): A) Site U1305 *C. wuellerstorfi* $\delta^{13}C$ values of tests visually cleaned using a brush and distilled water ('brush-cleaned'; sample average; x-axis) plotted versus tests cleaned using the standard protocol involving methanol (yellow circles), Site U1305 *C. wuellerstorfi* $\delta^{13}C$ values of brush-cleaned versus brush-cleaned tests (red circles), and MD03-2664 *C. wuellerstorfi* $\delta^{13}C$ values of standard-cleaned vs. standard-cleaned tests (blue circles; *10*). B) Same as in A) but for *C. wuellerstorfi* $\delta^{18}O$. Note the similarity in stable isotope values for the different cleaning protocols. C) Umbilical (left), apertural (middle), and spiral view (right) of an example specimen of *C. wuellerstorfi sensu stricto* from Site U1305 Hole C, 8H-3, 100-102 cm.

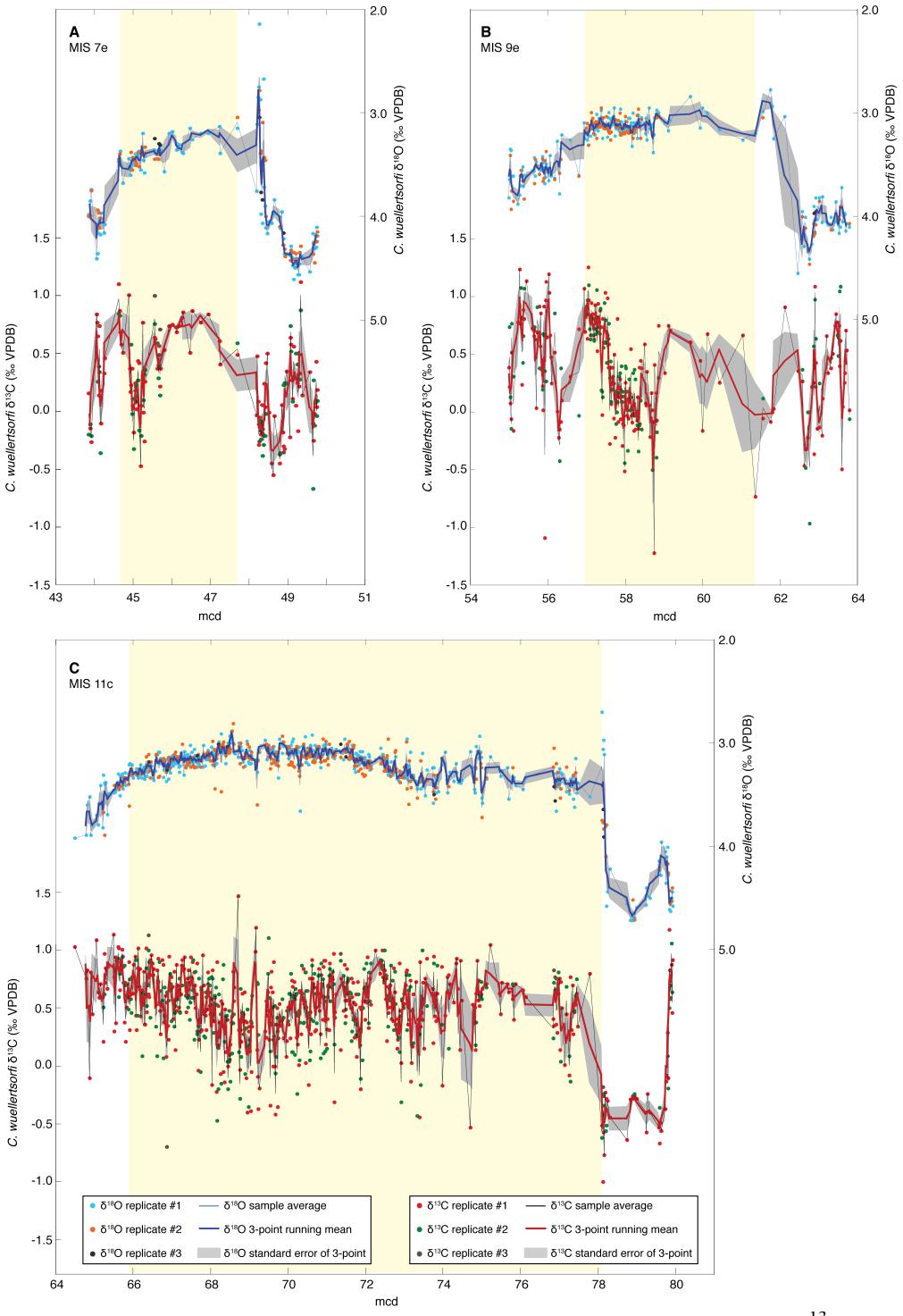

Fig. S2. Stable isotope results. The Site U1305 *C. wuellerstorfi* $\delta^{13}C$ (red) and $\delta^{18}O$ (blue) records for A) MIS 7e, B) MIS 9e, and C) MIS 11c plotted versus core depth (meter composite depth; mcd) showing all individual data points (dots; see inset at bottom for color coding), the sample average values (thin lines), the three-point running mean (bold lines), and the standard error of the mean of the three-point running window (gray shading; includes on average five individual data points).

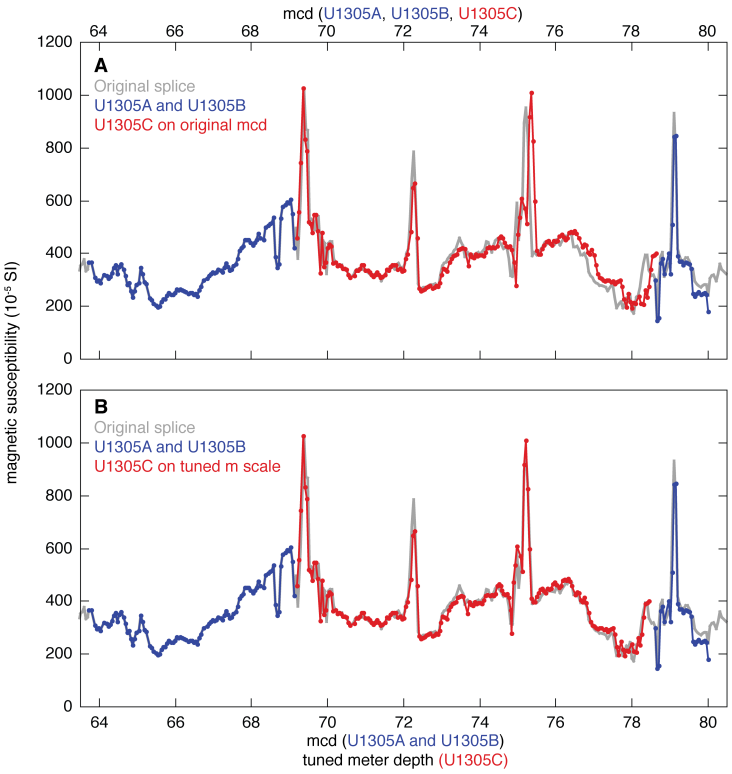

Fig. S3. Hole U1305C MIS 11c meter depth scale tuning. A) Magnetic susceptibility (*54*) of the original splice (gray) and our sampled intervals of U1305A and U1305B (blue) and U1305C (red) on the original mcd scale. Note the offset between U1305C and the original splice over ~74.5-78.5 mcd. B) Magnetic susceptibility (*54*) of the original splice (gray) and our sampled intervals of U1305A and U1305B (blue) on mcd, and our sampled interval of U1305C (red) on the tuned meter depth scale.

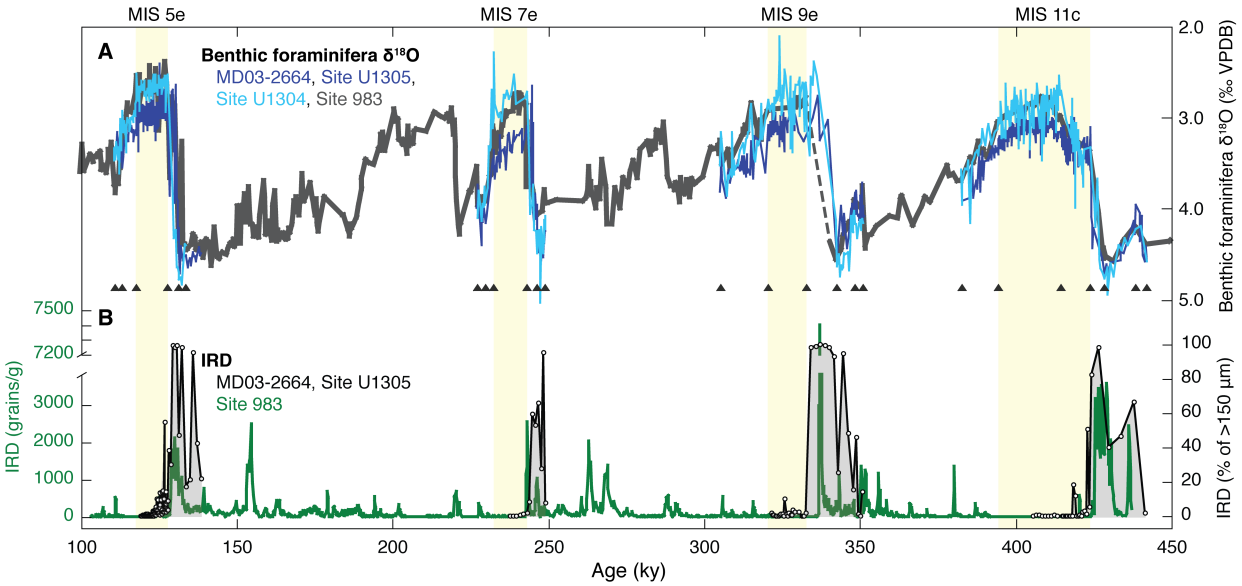

Fig. S4. Age model correlation. Plotted on LR04 age (ky): A) Benthic foraminifera $\delta^{18}O$ from MD03-2664 (dark blue; MIS 5e) (*10*), Site U1305 (dark blue; MIS 7e, 9e, and 11c), Site U1304 (light blue) (*15, 38*), and age model correlation target Site 983 (gray) (*33*) with tie points denoted by triangles; B) Site 983 ice-rafted debris (IRD) as grains gram^{-1} (*45*) compared to NW Atlantic IRD (black with gray shading) from MD03-2664 (MIS 5e) (*55*) and Site U1305 as percent IRD grains in total entities >150 μm shown only for the deglacial intervals where it was used to guide the age model construction. Dashed line in A) marks a prolonged interval lacking Site 983 $\delta^{18}O$ data across the MIS 10 to 9e transition. Yellow shading denotes the interglacial $\delta^{18}O$ plateaus as in the main text.

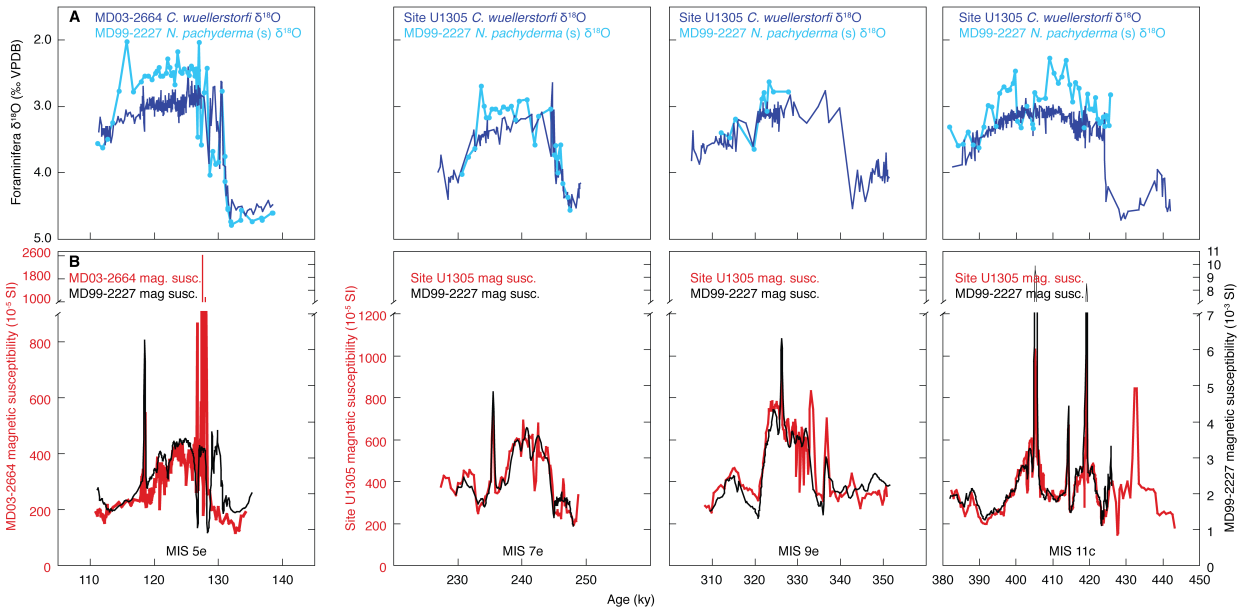

Fig. S5. Magnetic susceptibility correlation of MD03-2664/Site U1305 and MD99-2227. Plotted on the LR04 age scale obtained from transferring our $\delta^{18}O$-based age models of MD03-2664 (MIS 5e) and Site U1305 (MIS 7e, 9e, and 11c) to MD99-2227 by correlating magnetic susceptibility: A) epibenthic foraminifera *C. wuellerstorfi* $\delta^{18}O$ from core MD03-2664 (dark blue; MIS 5e) (*10*) and Site U1305 (dark blue; MIS 7e, 9e, and 11c) and planktic *N. pachyderma* (s) from core MD99-2227 (light blue) (*32*); B) magnetic susceptibility for MD03-2664 (red; MIS 5e) (*56*), Site U1305 (red; MIS 7e, 9e, and 11c) (*54*), and MD99-2227 (black) (*47*).

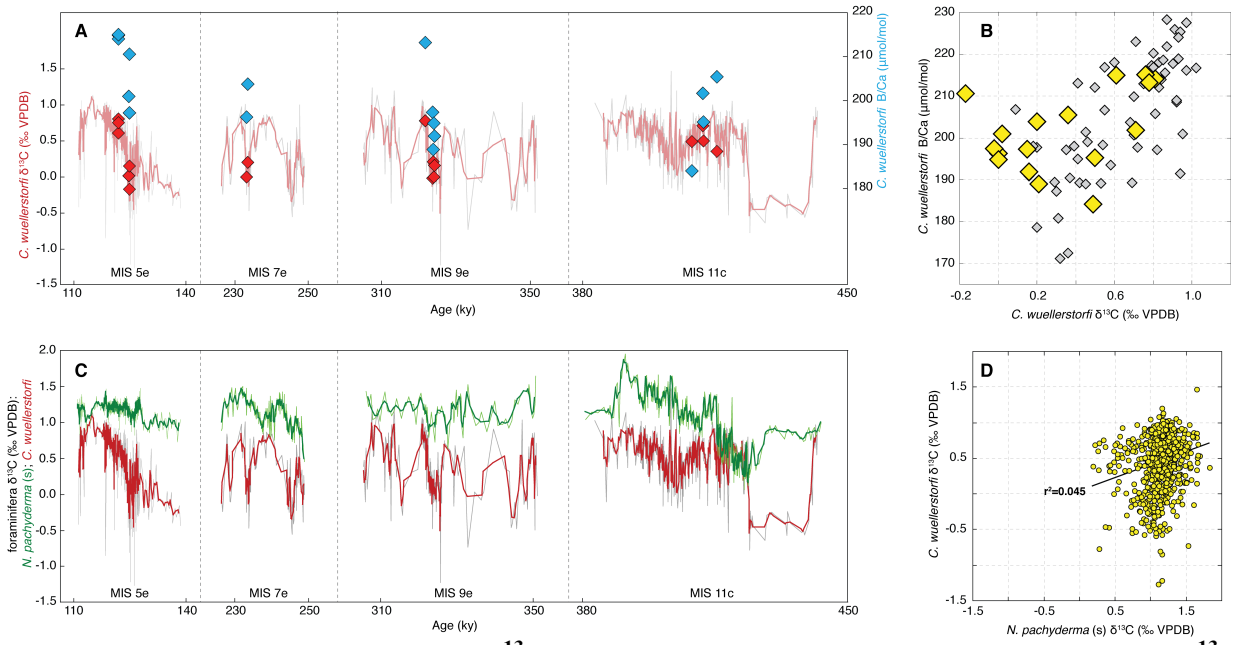

Fig. S6. Eirik Drift *C. wuellerstorfi* δ^{13}C, *C. wuellerstorfi* B/Ca, and *N. pachyderma* (s) δ^{13}C. A) The Eirik Drift *C. wuellerstorfi* B/Ca values (blue diamonds) of tests combined from selected intervals in MIS 5e (core MD03-2664), 7e, 9e, and 11c (Site U1305), the average δ^{13}C values of *C. wuellerstorfi* in the same intervals (red diamonds), and the full *C. wuellerstorfi* δ^{13}C time series shaded in the background for comparison (thin gray line, sample average; bold red line: 3-point running mean) over MIS 5e (MD03-2664; *10*), 7e, 9e, and 11c (Site U1305) plotted versus age (ky; LR04). B) Cross-plot of the Eirik Drift *C. wuellerstorfi* δ^{13}C and B/Ca data (yellow diamonds; comparing the red and blue diamonds from A)) compared to the equivalent data of the last glacial-to-Holocene intervals of cores BOFS 5K (50°42'N, 21°54'W; 3547 m w.d.; B/Ca from *C. wuellerstorfi* and *C. mundulus*; δ^{13}C from *Cibicidoides* spp.) and BOFS 8K (52°30'N, 22°06'W; 4045 m w.d.; B/Ca from *C. wuellerstorfi* and *C. mundulus*; δ^{13}C from *C. wuellerstorfi*) (gray diamonds; B/Ca data from Yu et al. (*52*), adjusted by +5% to correct for inter-laboratory differences; δ^{13}C data from Yu et al. (*52*) and references therein). C) The Eirik Drift *C. wuellerstorfi* δ^{13}C (coloring and references as in A)) and *N. pachyderma* (s) δ^{13}C from MIS 5e (MD03-2664; *55*) and MIS 7e, 9e, and 11c (Site U1305; this study). The *N. pachyderma* (s) data were corrected by +1.0‰ to account for disequilibrium (*57*). D) Cross-plot of Eirik Drift *N. pachyderma* (s) δ^{13}C (also corrected by +1.0‰) versus *C. wuellerstorfi* δ^{13}C (sample average values; data and references as in C)) where the solid line shows the linear fit (r^2=0.045).

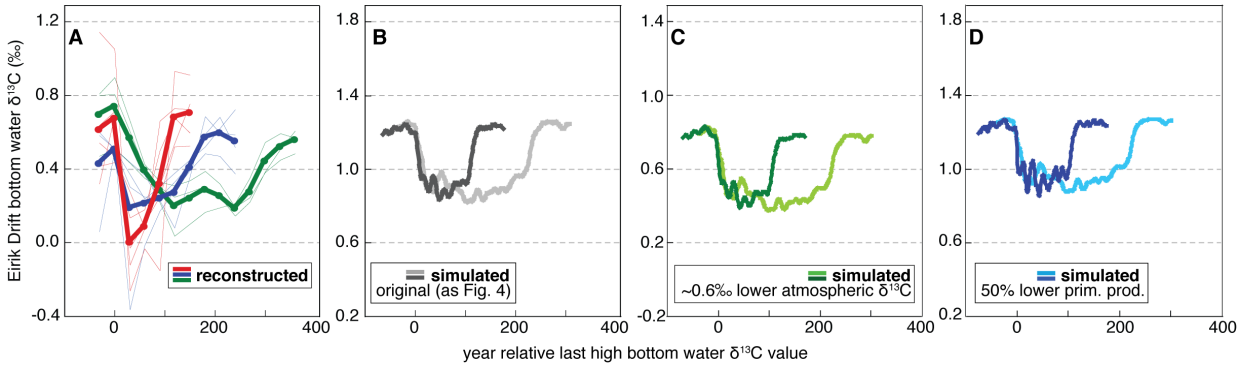

Fig. S7. Reconstructed and simulated Eirik Drift bottom water $\delta^{13}C$ variability. Plotted versus years relative the final high values preceding distinct bottom water $\delta^{13}C$ reductions at the Eirik Drift: A) reconstructed bottom water (*C. wuellerstorfi*) $\delta^{13}C$ changes shown as averages (bold lines) of individual events from MIS 1, 5e, 9e, and 11c (thin lines) at 30-year steps (obtained by linear interpolation) and binned according to durations of <100 (red; n=5), 101-200 (blue; n=4), and 201-300 years (green; n=3); for the same two simulated NADW shoaling events (showing ten-year running means): B) the original simulation as shown in Fig. 4; C) the original simulation but with atmospheric $\delta^{13}C$ decreased by ~0.6‰ and fixed (at -7.1‰); and D) the original simulation but with 50% decreased primary productivity in the northern deep water formation regions off southern Greenland and in the Nordic Seas.

Data S1. Eirik Drift stable isotope and B/Ca data (separate file)

The appended data file [Data S1_Eirik-Drift_MIS-7e-9e-11c.xlsx] includes: the IODP Site U1305 benthic foraminifera *C. wuellerstorfi* stable isotope data for MIS 7e, 9e, and 11c; the IODP Site U1305 planktic foraminifera *N. pachyderma* (s) $\delta^{13}C$ data for MIS 7e, 9e, and 11c; and the Eirik Drift benthic foraminifera *C. wuellerstorfi* B/Ca data for MIS 5e (core MD03-2664) and for MIS 7e, 9e, and 11c (IODP Site U1305).

References and Notes

1. T. F. Stocker, D. Qin, G.-K. Plattner, M. M. B. Tignor, S. K. Allen, J. Boschung, A. Nauels, Y. Xia, V. Bex, P. M. Midgley, Eds., *Climate Change 2013: The Physical Science Basis: Working Group I Contribution to the Fifth Assessment Report of the Intergovernmental Panel on Climate Change* (Cambridge Univ. Press, 2013).

2. M. W. Buckley, J. Marshall, Observations, inferences, and mechanisms of the Atlantic Meridional Overturning Circulation: A review. *Rev. Geophys.* **54**, 5–63 (2016). doi:10.1002/2015RG000493

3. C. L. Sabine, R. A. Feely, N. Gruber, R. M. Key, K. Lee, J. L. Bullister, R. Wanninkhof, C. S. Wong, D. W. Wallace, B. Tilbrook, F. J. Millero, T. H. Peng, A. Kozyr, T. Ono, A. F. Rios, The oceanic sink for anthropogenic CO2. *Science* **305**, 367–371 (2004). doi:10.1126/science.1097403 Medline

4. T. F. Stocker, A. Schmittner, Influence of CO2 emission rates on the stability of the thermohaline circulation. *Nature* **388**, 862–865 (1997). doi:10.1038/42224

5. H. Stommel, Thermohaline convection with two stable regimes of flow. *Tellus* **13**, 224–230 (1961). doi:10.3402/tellusa.v13i2.9491

6. T. F. Stocker, D. G. Wright, Rapid transitions of the ocean's deep circulation induced by changes in surface water fluxes. *Nature* **351**, 729–732 (1991). doi:10.1038/351729a0

7. M. Hofmann, S. Rahmstorf, On the stability of the Atlantic meridional overturning circulation. *Proc. Natl. Acad. Sci. U.S.A.* **106**, 20584–20589 (2009). doi:10.1073/pnas.0909146106 Medline

8. M. A. Srokosz, H. L. Bryden, Observing the Atlantic Meridional Overturning Circulation yields a decade of inevitable surprises. *Science* **348**, 1255575 (2015). doi:10.1126/science.1255575 Medline

9. M. S. Lozier, F. Li, S. Bacon, F. Bahr, A. S. Bower, S. A. Cunningham, M. F. de Jong, L. de Steur, B. deYoung, J. Fischer, S. F. Gary, B. J. W. Greenan, N. P. Holliday, A. Houk, L. Houpert, M. E. Inall, W. E. Johns, H. L. Johnson, C. Johnson, J. Karstensen, G. Koman, I. A. Le Bras, X. Lin, N. Mackay, D. P. Marshall, H. Mercier, M. Oltmanns, R. S. Pickart, A. L. Ramsey, D. Rayner, F. Straneo, V. Thierry, D. J. Torres, R. G. Williams, C. Wilson, J. Yang, I. Yashayaev, J. Zhao, A sea change in our view of overturning in the subpolar North Atlantic. *Science* **363**, 516–521 (2019). doi:10.1126/science.aau6592 Medline

10. E. V. Galaasen, U. S. Ninnemann, N. Irvalı, H. K. Kleiven, Y. Rosenthal, C. Kissel, D. A. Hodell, Rapid reductions in North Atlantic Deep Water during the peak of the last interglacial period. *Science* **343**, 1129–1132 (2014). doi:10.1126/science.1248667 Medline

11. J. F. Adkins, E. A. Boyle, L. Keigwin, E. Cortijo, Variability of the North Atlantic thermohaline circulation during the last interglacial period. *Nature* **390**, 154–156 (1997). doi:10.1038/36540

12. H. K. F. Kleiven, C. Kissel, C. Laj, U. S. Ninnemann, T. O. Richter, E. Cortijo, Reduced North Atlantic deep water coeval with the glacial Lake Agassiz freshwater outburst. *Science* **319**, 60–64 (2008). doi:10.1126/science.1148924 Medline

13. J. F. McManus, D. W. Oppo, J. L. Cullen, A 0.5-million-year record of millennial-scale climate variability in the north atlantic. *Science* **283**, 971–975 (1999). doi:10.1126/science.283.5404.971 Medline

14. D. W. Oppo, J. F. McManus, J. L. Cullen, Abrupt climate events 500,000 to 340,000 years ago: Evidence from subpolar north atlantic sediments. *Science* **279**, 1335–1338 (1998). doi:10.1126/science.279.5355.1335 Medline

15. D. A. Hodell, E. K. Minth, J. H. Curtis, I. N. McCave, I. R. Hall, J. E. T. Channell, C. Xuan, Surface and deep-water hydrography on Gardar Drift (Iceland Basin) during the last interglacial period. *Earth Planet. Sci. Lett.* **288**, 10–19 (2009). doi:10.1016/j.epsl.2009.08.040

16. A. de Vernal, C. Hillaire-Marcel, Natural variability of Greenland climate, vegetation, and ice volume during the past million years. *Science* **320**, 1622–1625 (2008). doi:10.1126/science.1153929 Medline

17. Past Interglacials Working Group of PAGES, Interglacials of the last 800,000 years. *Rev. Geophys.* **54**, 162–219 (2016). doi:10.1002/2015RG000482

18. A. V. Reyes, A. E. Carlson, B. L. Beard, R. G. Hatfield, J. S. Stoner, K. Winsor, B. Welke, D. J. Ullman, South Greenland ice-sheet collapse during Marine Isotope Stage 11. *Nature* **510**, 525–528 (2014). doi:10.1038/nature13456 Medline

19. See the supplementary materials.

20. A. Schmittner, H. C. Bostock, O. Cartapanis, W. B. Curry, H. L. Filipsson, E. D. Galbraith, J. Gottschalk, J. C. Herguera, B. Hoogakker, S. L. Jaccard, L. E. Lisiecki, D. C. Lund, G. Martínez-Méndez, J. Lynch-Stieglitz, A. Mackensen, E. Michel, A. C. Mix, D. W. Oppo, C. D. Peterson, J. Repschläger, E. L. Sikes, H. J. Spero, C. Waelbroeck, Calibration of the carbon isotope composition (δ13C) of benthic foraminifera. *Paleoceanography* **32**, 512–530 (2017). doi:10.1002/2016PA003072

21. B. Corliss, X. Sun, C. Brown, W. Showers, Influence of seasonal primary productivity on δ13C of North Atlantic deep-sea benthic foraminifera. *Deep Sea Res. Part I Oceanogr. Res. Pap.* **53**, 740–746 (2006). doi:10.1016/j.dsr.2006.01.006

22. M. Eide, A. Olsen, U. S. Ninnemann, T. Johannessen, A global ocean climatology of preindustrial and modern ocean δ13C. *Global Biogeochem. Cycles* **31**, 515–534 (2017). doi:10.1002/2016GB005473

23. L. E. Lisiecki, M. E. Raymo, W. B. Curry, Atlantic overturning responses to Late Pleistocene climate forcings. *Nature* **456**, 85–88 (2008). doi:10.1038/nature07425 Medline

24. L. G. Henry, J. F. McManus, W. B. Curry, N. L. Roberts, A. M. Piotrowski, L. D. Keigwin, North Atlantic ocean circulation and abrupt climate change during the last glaciation. *Science* **353**, 470–474 (2016). doi:10.1126/science.aaf5529 Medline

25. N. Bouttes, D. M. Roche, V. Mariotti, L. Bopp, Including an ocean carbon cycle model into iLOVECLIM (v1.0). *Geosci. Model Dev.* **8**, 1563–1576 (2015). doi:10.5194/gmd-8-1563-2015

26. J. F. McManus, R. Francois, J. M. Gherardi, L. D. Keigwin, S. Brown-Leger, Collapse and rapid resumption of Atlantic meridional circulation linked to deglacial climate changes. *Nature* **428**, 834–837 (2004). doi:10.1038/nature02494 Medline

27. R. Ferrari, M. F. Jansen, J. F. Adkins, A. Burke, A. L. Stewart, A. F. Thompson, Antarctic sea ice control on ocean circulation in present and glacial climates. *Proc. Natl. Acad. Sci. U.S.A.* **111**, 8753–8758 (2014). doi:10.1073/pnas.1323922111 Medline

28. G. Vettoretti, W. R. Peltier, Fast Physics and Slow Physics in the Nonlinear Dansgaard–Oeschger Relaxation Oscillation. *J. Clim.* **31**, 3423–3449 (2018). doi:10.1175/JCLI-D-17-0559.1

29. B. Martrat, J. O. Grimalt, N. J. Shackleton, L. de Abreu, M. A. Hutterli, T. F. Stocker, Four climate cycles of recurring deep and surface water destabilizations on the Iberian margin. *Science* **317**, 502–507 (2007). doi:10.1126/science.1139994 Medline

30. C. R. W. Ellison, M. R. Chapman, I. R. Hall, Surface and deep ocean interactions during the cold climate event 8200 years ago. *Science* **312**, 1929–1932 (2006). doi:10.1126/science.1127213 Medline

31. J. A. L. Nicholl, D. A. Hodell, B. D. A. Naafs, C. Hillaire-Marcel, J. E. T. Channell, O. E. Romero, A Laurentide outburst flooding event during the last interglacial period. *Nat. Geosci.* **5**, 901–904 (2012). doi:10.1038/ngeo1622

32. R. G. Hatfield, A. V. Reyes, J. S. Stoner, A. E. Carlson, B. L. Beard, K. Winsor, B. Welke, Interglacial responses of the southern Greenland ice sheet over the last 430,000 years determined using particle-size specific magnetic and isotopic tracers. *Earth Planet. Sci. Lett.* **454**, 225–236 (2016). doi:10.1016/j.epsl.2016.09.014

33. M. E. Raymo, D. W. Oppo, B. P. Flower, D. A. Hodell, J. F. McManus, K. A. Venz, K. F. Kleiven, K. McIntyre, Stability of North Atlantic water masses in face of pronounced climate variability during the Pleistocene. *Paleoceanography* **19**, PA2008 (2004). doi:10.1029/2003PA000921

34. L. E. Lisiecki, M. E. Raymo, A Pliocene-Pleistocene stack of 57 globally distributed benthic $\delta^{18}O$ records. *Paleoceanography* **20**, PA1003 (2005). doi:10.1029/2004PA001071

35. J. Laskar, P. Robutel, F. Joutel, M. Gastineau, A. C. M. Correia, B. Levrard, A long-term numerical solution for the insolation quantities of the Earth. *Astron. Astrophys.* **428**, 261–285 (2004). doi:10.1051/0004-6361:20041335

36. E. J. Colville, A. E. Carlson, B. L. Beard, R. G. Hatfield, J. S. Stoner, A. V. Reyes, D. J. Ullman, Sr-Nd-Pb isotope evidence for ice-sheet presence on southern Greenland during the Last Interglacial. *Science* **333**, 620–623 (2011). doi:10.1126/science.1204673 Medline

37. L. E. Lisiecki, A simple mixing explanation for late Pleistocene changes in the Pacific-South Atlantic benthic δ13C gradient. *Clim. Past* **6**, 305–314 (2010). doi:10.5194/cp-6-305-2010

38. C. Xuan, J. E. T. Channell, D. A. Hodell, Quaternary magnetic and oxygen isotope stratigraphy in diatom-rich sediments of the southern Gardar Drift (IODP Site U1304, North Atlantic). *Quat. Sci. Rev.* **142**, 74–89 (2016). doi:10.1016/j.quascirev.2016.04.010

39. C. Hillaire-Marcel, A. de Vernal, J. McKay, Foraminifer isotope study of the Pleistocene Labrador Sea, northwest North Atlantic (IODP Sites 1302/03 and 1305), with emphasis on paleoceanographical differences between its "inner" and "outer" basins. *Mar. Geol.* **279**, 188–198 (2011). doi:10.1016/j.margeo.2010.11.001

40. D. A. Hodell, J. H. Curtis, Oxygen and carbon isotopes of detrital carbonate in North Atlantic Heinrich Events. *Mar. Geol.* **256**, 30–35 (2008). doi:10.1016/j.margeo.2008.09.010

41. Y. Rosenthal, M. P. Field, R. M. Sherrell, Precise determination of element/calcium ratios in calcareous samples using sector field inductively coupled plasma mass spectrometry. *Anal. Chem.* **71**, 3248–3253 (1999). doi:10.1021/ac981410x Medline

42. N. Irvalı, E. V. Galaasen, U. S. Ninnemann, Y. Rosenthal, A. Born, H. K. F. Kleiven, A low climate threshold for south Greenland Ice Sheet demise during the Late Pleistocene. *Proc. Natl. Acad. Sci. U.S.A.* **117**, 190–195 (2020). doi:10.1073/pnas.1911902116 Medline

43. H. Goosse, V. Brovkin, T. Fichefet, R. Haarsma, P. Huybrechts, J. Jongma, A. Mouchet, F. Selten, P.-Y. Barriat, J.-M. Campin, E. Deleersnijder, E. Driesschaert, H. Goelzer, I. Janssens, M.-F. Loutre, M. A. Morales Maqueda, T. Opsteegh, P.-P. Mathieu, G. Munhoven, E. J. Pettersson, H. Renssen, D. M. Roche, M. Schaeffer, B. Tartinville, A. Timmermann, S. L. Weber, Description of the Earth system model of intermediate complexity LOVECLIM version 1.2. *Geosci. Model Dev.* **3**, 603–633 (2010). doi:10.5194/gmd-3-603-2010

44. F. J. Millero, Thermodynamics of the carbon dioxide system in the oceans. *Geochim. Cosmochim. Acta* **59**, 661–677 (1995). doi:10.1016/0016-7037(94)00354-O

45. S. Barker, J. Chen, X. Gong, L. Jonkers, G. Knorr, D. Thornalley, Icebergs not the trigger for North Atlantic cold events. *Nature* **520**, 333–336 (2015). doi:10.1038/nature14330 Medline

46. L. C. Skinner, N. J. Shackleton, Deconstructing Terminations I and II: Revisiting the glacioeustatic paradigm based on deep-water temperature estimates. *Quat. Sci. Rev.* **25**, 3312–3321 (2006). doi:10.1016/j.quascirev.2006.07.005

47. H. F. Evans, J. E. T. Channell, J. S. Stoner, C. Hillaire-Marcel, J. D. Wright, L. C. Neitzke, G. S. Mountain, Paleointensity-assisted chronostratigraphy of detrital layers on the Eirik Drift (North Atlantic) since marine isotope stage 11. *Geochem. Geophys. Geosyst.* **8**, Q11007 (2007). doi:10.1029/2007GC001720

48. C. Hillaire-Marcel, A. Vernal, G. Bilodeau, G. Wu, Isotope stratigraphy, sedimentation rates, deep circulation, and carbonate events in the Labrador Sea during the last ~200 ka. *Can. J. Earth Sci.* **31**, 63–89 (1994). doi:10.1139/e94-007

49. J. S. Stoner, J. E. Channell, C. Hillaire-Marcel, The magnetic signature of rapidly deposited detrital layers from the deep Labrador Sea: Relationship to North Atlantic Heinrich layers. *Paleoceanography* **11**, 309–325 (1996). doi:10.1029/96PA00583

50. A. E. Carlson, J. S. Stoner, J. P. Donnelly, C. Hillaire-Marcel, Response of the southern Greenland Ice Sheet during the last two deglaciations. *Geology* **36**, 359–362 (2008). doi:10.1130/G24519A.1

51. J. Yu, H. Elderfield, Benthic foraminiferal B/Ca ratios reflect deep water carbonate saturation state. *Earth Planet. Sci. Lett.* **258**, 73–86 (2007). doi:10.1016/j.epsl.2007.03.025

52. J. Yu, H. Elderfield, A. M. Piotrowski, Seawater carbonate ion-δ13C systematics and application to glacial–interglacial North Atlantic ocean circulation. *Earth Planet. Sci. Lett.* **271**, 209–220 (2008). doi:10.1016/j.epsl.2008.04.010

53. T. Fronval, E. Jansen, H. Haflidason, H. P. Sejrup, Variability in surface and deep water conditions in the nordic seas during the last interglacial period. *Quat. Sci. Rev.* **17**, 963–985 (1998). doi:10.1016/S0277-3791(98)00038-9

54. J. E. T. Channell, T. Kanamatsu, T. Sato, R. Stein, C. A. Alvarez Zarikian, M. J. Malone, the Expedition 303 Scientists, in *Expedition 303 Summary*. Proceedings of the Integrated Ocean Drilling Program, vol. 303/306 (IODP, 2006). doi:10.2204/iodp.proc.303306.101.2006

55. N. Irvalı, U. S. Ninnemann, E. V. Galaasen, Y. Rosenthal, D. Kroon, D. W. Oppo, H. F. Kleiven, K. F. Darling, C. Kissel, Rapid switches in subpolar North Atlantic hydrography and climate during the Last Interglacial (MIS 5e). *Paleoceanography* **27**, PA2207 (2012). doi:10.1029/2011PA002244

56. C. Laj, X. Morin, the Shipboard Scientific Party, MD132-P.I.C.A.S.S.O/IMAGES XI cruise report, Les rapports de campagne à la mer (no. OCE/2004/02, 2004).

57. K. E. Kohfeld, R. G. Fairbanks, S. L. Smith, I. D. Walsh, Neogloboquadrina pachyderma (sinistral coiling) as paleoceanographic tracers in polar oceans: Evidence from Northeast Water Polynya plankton tows, sediment traps, and surface sediments. *Paleoceanography* **11**, 679–699 (1996). doi:10.1029/96PA02617